# Compliant riblets: Problem formulation and effective macrostructural properties

Giuseppe A Zampogna, Sahrish B Naqvi, Jacques Magnaudet, Alessandro Bottaro

Available online at www.sciencedirect.com
ScienceDirect
Journal Fluids Structures 00 (2018) 1–13
Journal Fluids Structures

# Compliant riblets: problem formulation and effective macrostructural properties

Giuseppe A. Zampogna[1a], Sahrish B. Naqvi[b], Jacques Magnaudet[a], Alessandro Bottaro[b]

[a] *Institut de Mécanique des Fluides de Toulouse (IMFT), Université de Toulouse, CNRS, INPT, UPS, Toulouse, France*
[b] *Dipartimento di Ingegneria Civile, Chimica e Ambientale, Università di Genova, Via Montallegro 1, Genova, 16145, Italy*

**Abstract**

*Keywords:*

## 1. Introduction

Riblets are elongated micro-grooves at the wall, aligned with the direction of the main flow. They represent a mature passive control technology aimed at reducing skin friction drag in turbulent flow, which has been successfully tested both in the laboratory and in aeronautical/marine applications. The mechanism by which riblets operate is by-now well understood and consists in the creation of an offset between the virtual origin of the longitudinal mean flow and that of the transverse turbulent eddies. Provided that the riblets are embedded in the viscous sublayer, their effect can be modeled by the Stokes equation to yield two *protrusion heights*, or *Navier's slip lengths*, longitudinal, $\lambda_1$, and transverse, $\lambda_2$, which are the distances from the rim of the riblets to the position where, respectively, streamwise and cross-stream flows originate. These concepts have been introduced by Bechert and Bartenwerfer [1] and Luchini *et al.* [2], and tested experimentally by Bechert *et al.* [3], among others. The results show that riblets remain in the linear (Stokes) regime as long as their dimensionless spanwise periodicity, $s^+$, measured in viscous wall units, remains below a value close to 12. The optimal riblet spacing is close to 15 for a variety of riblet shapes, and skin friction drag can be reduced by at the most 10% in the case of thin, blade-like riblets [3]. Above $s^+ \approx 15$ drag starts increasing again and for $s^+ \gtrsim 20$ the skin friction coefficient exceeds the value of the corresponding smooth wall because of the appearance of a Kelvin-Helmholtz-like instability of the mean flow which increases the spanwise coherence of the turbulent structures, in so doing destructuring the longitudinal streaks, *via* the creation of spanwise rollers [4].

For drag to decrease, for any kind of wall indentation fully immersed in the viscous sublayer, the origin of the secondary flow must be further away from the base of the indentation than the origin of the mean streamwise motion or, in other words, $\Delta\lambda = \lambda_1 - \lambda_2$ must be positive. The amount by which this is achieved is given by

$$\frac{\Delta C_f}{C_{f_0}} = -\frac{\Delta\lambda^+}{(2\,C_{f_0})^{-1/2} + (2\kappa)^{-1}} \tag{1}$$

as first shown by Luchini [5]. In equation (1), $C_f$ is the skin friction coefficient, $C_{f_0}$ its value for the case of a smooth surface under the same outer flow conditions, and $\kappa = 4.48$ is von Kármán's constant [6]. Despite the fact that the

[1] Present affiliation: LFMI, Ecole Polytechnique Fédérale de Lausanne, CH-1015, Lausanne, Switzerland

equation above holds only in the initial part of the drag curve (*i.e.* until the spanwise spacing of the micro-grooves is below 12 wall units), the agreement of this theoretical estimate with experiments is very good and strongly endorses the idea of maximizing $\Delta\lambda$ when drag reduction is sought for.

Clearly the optimal geometrical characteristics of the riblets depend on the outer flow conditions, and what is optimal for one condition (say, level flight of an aircraft at cruise speed) may not be optimal any more under different conditions. Recently, a patent has been submitted describing the manufacturing of elastomeric riblets [7], with the claim that their optimized structural design provides the capability for riblets to be "thinner, lower weight and more aerodynamically efficient". It thus becomes interesting to examine the interaction between elastic micro-structures anchored at the wall and the overlying fluid. We call these wall indentation *compliant riblets*.

This contribution is dedicated to the study of the microscopic problems, for the fluid and for the solid domains, characterizing triangular riblets made of a linearly elastic material. The main outcome of the work will be the macroscopic equations ruling the interaction, and the effective coefficients (or convolution kernels, by virtue of the time dependent nature of the fluid-solid coupling) required to close the macroscopic problem.

## 2. Model development

The flow of an incompressible Newtonian fluid of density $\rho_f$ and viscosity $\mu$ is assumed to flow over a microstructured surface made of a linearly elastic material of density $\rho_s$, Poisson's ratio $\nu_P$ and Young's modulus $E$. A sketch of the surface being considered is represented in figure 1. The objective of this model is to simulate the fluid flow and solid structure deformation without the need of large computational efforts to describe the details of the solid surface and solve the small-scale fluid-solid interactions. The procedure shown in the present section gives rise to equivalent boundary conditions for the macroscopic fields associated with the solid displacement and fluid flow. These boundary conditions must be imposed on an equivalent smooth surface (denoted with $\mathbb{E}$ in figure 1) which is located at a certain (small) distance from the tip of the protrusions forming the microstructured surface. To proceed with the development of these conditions we introduce the fluid domain, denoted by $\mathbb{F}$ in figure 1, in which the incompressible Navier-Stokes equations are valid and write in dimensional form

$$\rho_f\left(\frac{\partial\hat{u}_i}{\partial\hat{t}}+\hat{u}_j\frac{\partial\hat{u}_i}{\partial\hat{x}_j}\right)=\frac{\partial\hat{\Sigma}_{ij}}{\partial\hat{x}_j}\,, \tag{2}$$

$$\frac{\partial\hat{u}_i}{\partial\hat{x}_i}=0\,, \tag{3}$$

where $\hat{\Sigma}_{ij}$ is the canonical fluid stress tensor of a Newtonian fluid

$$\hat{\Sigma}_{ij}=-\hat{p}\delta_{ij}+2\mu\hat{\varepsilon}_{ij}(\hat{\mathbf{u}})\,, \tag{4}$$

and $\hat{\varepsilon}_{ij}(\hat{\mathbf{u}})$ is the strain-rate tensor, formally defined as

$$\hat{\varepsilon}_{ij}(\hat{\mathbf{u}})=\frac{1}{2}\left(\frac{\partial\hat{u}_i}{\partial\hat{x}_j}+\frac{\partial\hat{u}_j}{\partial\hat{x}_i}\right). \tag{5}$$

In the domain $\mathbb{S}$ occupied by the linearly elastic solid, the governing equations read

$$\rho_s\frac{\partial^2\hat{v}_i}{\partial\hat{t}^2}=\frac{\partial\hat{\sigma}_{ij}}{\partial\hat{x}_j}, \tag{6}$$

where the components of the displacement vector, $\hat{\mathbf{v}}$, are $\hat{v}_i$, and $\hat{\sigma}_{ij}$ is the generic component of the stress tensor. Under the assumption that the structure is elastic, the stress and strain tensors are linearly related through the relation

$$\hat{\sigma}_{ij}=\hat{C}_{ijkl}\hat{\varepsilon}_{kl}(\hat{\mathbf{v}})=\frac{1}{2}\hat{C}_{ijkl}\left(\frac{\partial\hat{v}_k}{\partial\hat{x}_l}+\frac{\partial\hat{v}_l}{\partial\hat{x}_k}\right), \tag{7}$$

where $\hat{C}_{ijkl}=\hat{\lambda}\delta_{ij}\delta_{kl}+\hat{G}(\delta_{ik}\delta_{jl}+\delta_{il}\delta_{jk})$ is the stiffness tensor, and $\hat{\lambda}$ and $\hat{G}$ are the two Lamé coefficients. These coefficients are related to the Young modulus, $E$, and Poisson's ratio, $\nu_p$, as $\hat{\lambda}=\dfrac{\nu_p E}{(1+\nu_p)(1-2\nu_p)}$ and $\hat{G}=\dfrac{E}{2(1+\nu_p)}$.

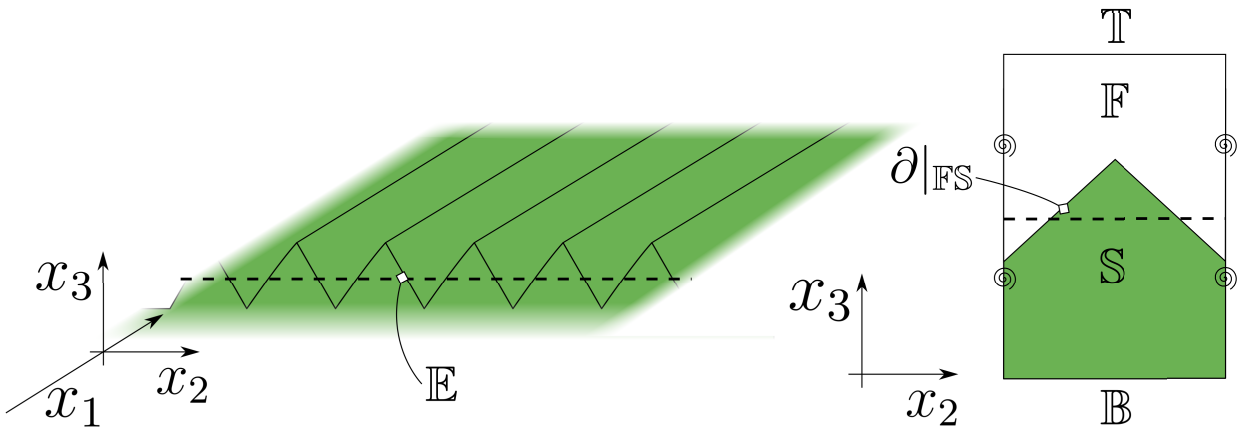


Figure 1. Sketch of a deformable microstructured surface. Right frame: a periodic unit cell is identified to apply the homogenization technique. In the present case, a cuboid of dimensions $\epsilon \times \epsilon \times 2\epsilon$ is selected.

The fluid and solid equations are coupled through the matching of velocities and tractions across the microscopic fluid-solid interface denoted with $\partial|_{\mathbb{FS}}$, *viz.*

$$\hat{u}_i = \frac{\partial \hat{v}_i}{\partial \hat{t}}\,, \tag{8}$$

and

$$\hat{\Sigma}_{ij} n_j = \hat{\sigma}_{ij} n_j\,. \tag{9}$$

We also need to specify the boundary conditions at the bottom $\mathbb{B}$, and top $\mathbb{T}$ of the unit cell sketched in figure 1. Continuity of fluid tractions and velocity is imposed on $\mathbb{T}$, i.e.

$$\hat{\Sigma}_{ij} n_j = \hat{\Sigma}^{out}_{ij} n_j \quad \text{and} \quad \hat{u}_i = \hat{u}^{out}_i\,, \tag{10}$$

where the superscript $^{out}$ denotes the variables on the external side of the cell, cf. [8]. It is also assumed that the unit normal vector points out of the solid and into the fluid. On $\mathbb{B}$ we impose that

$$\hat{v}_i = 0\,, \tag{11}$$

which is equivalent to assuming that the elastic layer is anchored to a rigid, undeformable substrate.

### *2.1. Scaling relations*

We start by assuming that the continuum layer made up by fluid and solid is characterized by a frequency, $\mathsf{f}$, sufficiently large for dynamic effects to be felt at leading order. Then, it can be argued that in the fluid domain

$$\rho_f U \mathsf{f} \sim \frac{P}{l} \sim \mu \frac{U}{l^2}, \tag{12}$$

with $U$ the velocity scale, $P$ the pressure scale, and $l$ the microscopic length scale. From the above, we can choose the velocity scale to normalize the equations, i.e.

$$U = \frac{P\, l}{\mu}. \tag{13}$$

We further have a relation between the microscale $l$ and the frequency $\mathsf{f}$, which states that, for viscous effects to balance inertia, $l$ must be of the order of the Stokes layer thickness, i.e.

$$l = \sqrt{\frac{\mu}{\rho_f \mathsf{f}}}. \tag{14}$$

The small displacement of the elastic riblets is assumed to occur coherently over a macroscopic length $L$. This is the case, for instance, of *honami* waves of canopy flows. By equilibrating inertia and diffusion in Cauchy's equation for the solid, we have

$$\rho_s \mathcal{V} \mathsf{f}^2 \sim E \frac{\mathcal{V}}{L^2}, \tag{15}$$

so that the macroscale $L$ can be taken to coincide with the elastic wavelength, i.e.

$$L = \frac{1}{\mathsf{f}} \sqrt{\frac{E}{\rho_s}}. \tag{16}$$

The interface conditions (8) is useful since it permits to relate the displacement and the velocity scales, i.e.

$$U = \mathsf{f} \mathcal{V}. \tag{17}$$

We are ready to introduce the relations between the dimensional and dimensionless variables (the latter without hat), setting

$$\hat{t} = \frac{t}{\mathsf{f}}, \quad \hat{\mathbf{x}} = l\,\mathbf{x}, \quad \hat{p} = P p, \quad \hat{\mathbf{u}} = \frac{P\,l}{\mu}\,\mathbf{u}, \quad \hat{\mathbf{v}} = \frac{P\,l}{\mu\,\mathsf{f}}\,\mathbf{v}\,. \tag{18}$$

Substituting these definitions in the continuity and momentum equations for the fluid phase, we obtain

$$\frac{\partial u_i}{\partial x_i} = 0\,; \quad \frac{\partial u_i}{\partial t_f} + \mathrm{Re}\, u_j \frac{\partial u_i}{\partial x_j} = -\frac{\partial p}{\partial x_i} + 2\frac{\partial \varepsilon_{ij}(\mathbf{u})}{\partial x_j} \quad \text{in } \mathbb{F}\,, \tag{19}$$

where $\varepsilon_{ij}(\mathbf{u}) = \dfrac{1}{2}\left[\dfrac{\partial u_i}{\partial x_j} + \dfrac{\partial u_j}{\partial x_i}\right]$ and $\mathrm{Re} = \dfrac{\rho_f U l}{\mu} = \epsilon \mathcal{R}$, with $\mathcal{R} = \dfrac{\rho_f U L}{\mu}$, assuming the microscale Reynolds number Re to be of order $\epsilon$ (or possibly smaller). Applying the same procedure to the Cauchy's equation in the solid we obtain

$$\epsilon^2 \frac{\partial^2 v_i}{\partial t^2} = \frac{\partial \sigma_{ij}}{\partial x_j} \quad \text{in } \mathbb{S}\,, \tag{20}$$

with $\sigma_{ij} = C_{ijkl}\varepsilon_{kl}(\mathbf{v})$ and $C_{ijkl} = \hat{C}_{ijkl}/E$. The continuity of tractions on $\partial|_{\mathbb{FS}}$ becomes

$$-p\,n_i + 2\varepsilon_{ij}(\mathbf{u})\,n_j = \epsilon^{-2}\,\frac{\rho_s}{\rho_f}\,C_{ijkl}\,\varepsilon_{kl}(\mathbf{v})\,n_j\,, \tag{21}$$

and the kinematic condition reads

$$u_i = \frac{\partial v_i}{\partial t}\,. \tag{22}$$

The periodicity condition along $x_1$ and $x_2$ in the unit cell (fig. 1, right frame) must also be enforced, together with $v_i = 0$ at $\mathbb{B}$ and $\Sigma_{ij}\,n_j = \Sigma_{ij}^{out}\,n_j$ at $\mathbb{T}$.

### *2.2. Multiple scale expansion*

Within the microstructured elastic layer, we can use the multiscale homogenization approach described by Mei & Vernescu [9]. We introduce the fast (microscopic) and slow (macroscopic) variables, $\mathbf{x} = (x_1, x_2, x_3)$ and $\mathbf{x}' = \epsilon(x_1, x_2)$, and the expansions

$$\mathcal{F} = \sum_{i=0}^{\infty} \epsilon^i\,\mathcal{F}^{(i)}\,, \tag{23}$$

where $\mathcal{F}^{(i)} = (\mathbf{u}^{(i)}, \mathbf{v}^{(i)}, p^{(i)})$ is a function of $(\mathbf{x}, \mathbf{x}', t)$. The spatial derivatives become

$$\frac{\partial}{\partial x_i} \to \frac{\partial}{\partial x_i} + \epsilon\frac{\partial}{\partial x_i'} \qquad \text{for } i = 1, 2\,, \tag{24}$$

so that

$$\varepsilon_{ij}(\mathbf{u}) \to \varepsilon_{ij}(\mathbf{u}) + \epsilon\varepsilon'_{ij}(\mathbf{u})\,, \tag{25}$$

with $\varepsilon'_{ij}(\mathbf{u}) = \dfrac{1}{2}\left(\dfrac{\partial u_i}{\partial x'_j} + \dfrac{\partial u_j}{\partial x'_i}\right)$. The fact that the slow variable has a missing third entry results from the fact that the microstructured layer does not extend macroscopically along the normal-to-the-surface direction, $x_3$ (cf. figure 1). For simplicity we maintain the notation $x'_i$, with the understanding that $i$ can only be equal to 1 or 2. The fluid equations at order $\epsilon^0$ and $\epsilon^1$ in $\mathbb{F}$ then read

$$\frac{\partial u_i^{(0)}}{\partial x_i} = 0\,, \tag{26}$$

$$\frac{\partial u_i^{(1)}}{\partial x_i} + \frac{\partial u_i^{(0)}}{\partial x'_i} = 0\,, \tag{27}$$

$$\frac{\partial u_i^{(0)}}{\partial t} = \frac{\partial \Sigma_{ij}^{(0)}}{\partial x_j} = -\frac{\partial p^{(0)}}{\partial x_i} + \frac{\partial^2 u_i^{(0)}}{\partial x_k^2}\,, \tag{28}$$

$$\frac{\partial u_i^{(1)}}{\partial t} + \mathcal{R}\, u_j^{(0)} \frac{\partial u_i^{(0)}}{\partial x_j} = \frac{\partial \Sigma_{ij}^{(0)}}{\partial x'_j} + \frac{\partial \Sigma_{ij}^{(1)}}{\partial x_j}\,. \tag{29}$$

In (28) and (29) we have used the definition

$$\Sigma_{ij}^{(n)} = -p^{(n)}\delta_{ij} + 2\left[\varepsilon_{ij}(\mathbf{u}^{(n)}) + \varepsilon'_{ij}(\mathbf{u}^{(n-1)})\right]\,, \tag{30}$$

for each $n \geq 0$, with $\mathbf{u}^{(-1)} = 0$ for consistency. Similarly, the equations describing the motion of the solid structure at order $\epsilon^{-2}$, $\epsilon^{-1}$ and $\epsilon^0$ in the $\mathbb{S}$ domain are

$$\frac{\partial \sigma_{ij}^{(0)}}{\partial x_j} = 0\,, \tag{31}$$

$$0 = \frac{\partial \sigma_{ij}^{(1)}}{\partial x_j} + \frac{\partial \sigma_{ij}^{(0)}}{\partial x'_j}\,, \tag{32}$$

$$\frac{\partial^2 v_i^{(0)}}{\partial t^2} = \frac{\partial \sigma_{ij}^{(2)}}{\partial x_j} + \frac{\partial \sigma_{ij}^{(1)}}{\partial x'_j}\,. \tag{33}$$

In (32) and (33) the stress tensor at each order, $\sigma_{ij}^{(n)}$, is defined as

$$\sigma_{ij}^{(n)} = C_{ijkl}\left[\varepsilon_{kl}(\mathbf{v}^{(n)}) + \varepsilon'_{kl}(\mathbf{v}^{(n-1)})\right]\,, \tag{34}$$

for each $n \geq 0$, with $\mathbf{v}^{(-1)} = 0$ for consistency. On $\partial|_{\mathbb{FS}}$ the interface conditions read

$$u_i^{(0)} = \frac{\partial v_i^{(0)}}{\partial t}\,, \tag{35}$$

$$u_i^{(1)} = \frac{\partial v_i^{(1)}}{\partial t}\,, \tag{36}$$

$$\sigma_{ij}^{(0)} n_j = 0\,, \tag{37}$$

$$\sigma_{ij}^{(1)} n_j = 0, \tag{38}$$

$$\frac{\rho_s}{\rho_f}\,\sigma_{ij}^{(2)} n_j = \Sigma_{ij}^{(0)} n_j = -p^{(0)} n_i + 2\varepsilon_{ij}(\mathbf{u}^{(0)}) n_j\,. \tag{39}$$

To manage the boundary condition (10) on the top side of the cell, $\mathbb{T}$, we follow the same procedure as in [8], by truncating the continuity of tractions at order $\epsilon$, which in the present case yields

$$\Sigma^{(0)}_{ij} n_j + \epsilon \Sigma^{(1)}_{ij} n_j = \Sigma^{out}_{ij} n_j \quad \text{on } \mathbb{T}\,. \tag{40}$$

The outer stress tensor depends on the outer quantities defined in [8] (i.e. $\mathbf{x}^{out} = (x'_1, x'_2, x^{out}_3)$ with $x^{out}_3 = \epsilon x_3$) and is supposed not to be influenced by the small scales (this assumption is valid if $\mathbb{T}$ is sufficiently far from the elastic, microstructured wall). Collecting terms at each order in (40), we obtain

$$\Sigma^{(0)}_{ij} n_j = \Sigma^{out}_{ij} n_j \quad \text{on } \mathbb{T}\,, \tag{41}$$

and

$$\Sigma^{(1)}_{ij} n_j = 0 \quad \text{on } \mathbb{T}\,. \tag{42}$$

By the same arguments used in [8], it is also $\epsilon u^{(0)}_i = u^{out}_i$ at the upper boundary. Finally, the boundary condition (11) on $\mathbb{B}$ is merely a homogeneous Dirichlet condition for the displacement at each order. Other boundary conditions can be used on $\mathbb{B}$, such as a prescribed shear or normal stress to impose a specific time-varying deformation of the elastic layer.

### *2.3. The macroscopic model*

Equation (31) and the homogeneous boundary condition (37) imply that $v^{(0)}$ does not depend on the microscopic variable, i.e. $v^{(0)} = v^{(0)}(\mathbf{x}', t)$, so that $\sigma^{(0)}_{ij} = 0$. Equations (26) and (28) can then be written as

$$\frac{\partial}{\partial x_i}(u^{(0)}_i - \dot{v}^{(0)}_i) = 0\,, \tag{43}$$

$$\frac{\partial}{\partial t}(u^{(0)}_i - \dot{v}^{(0)}_i) = -\ddot{v}^{(0)}_i - \frac{\partial p^{(0)}}{\partial x_i} + \frac{\partial^2}{\partial x_k^2}(u^{(0)}_i - \dot{v}^{(0)}_i)\,, \tag{44}$$

and, out of linearity, the solution of (43) and (44) with boundary conditions (35) and (41) can be defined with four convolution kernels, $L_{ijk}(\mathbf{x}, t)$, $H_{ij}(\mathbf{x}, t)$, $B_{jk}(\mathbf{x}, t)$ and $A_j(\mathbf{x}, t)$, as:

$$u^{(0)}_i - \dot{v}^{(0)}_i = \int_0^t L_{ijk}(\mathbf{x}, t - t')\, \varepsilon'_{jk}(\mathbf{u}^{out}; t')\, dt' + \int_0^t H_{ij}(\mathbf{x}, t - t')\, \ddot{v}^{(0)}_j(\mathbf{x}', t')\, dt'\,, \tag{45}$$

$$p^{(0)} = \bar{p}^{(0)}(\mathbf{x}', t) + \int_0^t B_{jk}(\mathbf{x}, t - t')\, \varepsilon'_{jk}(\mathbf{u}^{out}; t')\, dt' + \int_0^t A_j(\mathbf{x}, t - t')\, \ddot{v}^{(0)}_j(\mathbf{x}', t')\, dt'\,, \tag{46}$$

where $\bar{p}^{(0)}$ is the macroscopic reference pressure which can be set thanks to the third component of (41). By substituting (45) and (46) into (43), (44), (35) and (41), the tensors $L_{ijk}$, $H_{ij}$, $B_{jk}$ and $A_j$ are found to satisfy the following microscopic problems:

$$\begin{cases} \dfrac{\partial L_{ijk}}{\partial t} = -\dfrac{\partial B_{jk}}{\partial x_i} + \nabla^2 L_{ijk} \quad \text{in} \quad \mathbb{F}\,, \\ \dfrac{\partial L_{ijk}}{\partial x_i} = 0 \quad \text{in} \quad \mathbb{F}\,, \\ L_{ijk} = 0 \quad \text{on} \quad \partial|_{\mathbb{FS}}\,, \\ \mathcal{U}(t')\, \mathcal{U}(t - t')\, \varepsilon_{ij}\left(L_{\cdot pq}(t - t')\right) n_j = \delta(t' - t)\, \delta_{ip}\, \delta_{jq}\, n_j \quad \text{on} \quad \mathbb{T}\,, \\ L_{ijk}, B_{jk} \quad \text{periodic along the tangential directions 1 and 2}\,, \end{cases} \tag{47}$$

$$\begin{cases} \dfrac{\partial H_{ij}}{\partial t} = -\dfrac{\partial A_j}{\partial x_i} + \nabla^2 H_{ij} \quad \text{in} \quad \mathbb{F}\,, \\ \dfrac{\partial H_{ij}}{\partial x_i} = 0 \quad \text{in} \quad \mathbb{F}\,, \\ H_{ij} = 0 \quad \text{on} \quad \partial|_{\mathbb{FS}}\,, \\ \varepsilon_{ij}(H_{\cdot p})\, n_j = 0 \quad \text{on} \quad \mathbb{T}\,, \\ H_{ij}, A_j \quad \text{periodic along the tangential directions 1 and 2}\,, \end{cases} \tag{48}$$

subject to the initial condition $L_{ijk}(\mathbf{x}, 0) = 0$ and $H_{ij}(\mathbf{x}, 0) = -\delta_{ij}$. In the boundary condition at the top of the domain, $\mathbb{T}$, for system (47), $\mathcal{U}(t - t')$ is the unit step function centered in $t'$ and $\delta(t)$ is Dirac's delta function. The solutions of interest are transients. In particular, since $\boldsymbol{L}$ solves problem (47) for each $t'$ greater than 0, it is univocally defined up to a temporal translation of $t'$. To carry out the numerical solution we set $t' = 0$.

At this point we introduce the spatial average over a unit cell to deduce macroscopic equations valid over the homogenized domain. The average is defined as

$$\langle f \rangle := \frac{1}{|\mathbb{F} \cup \mathbb{S}|} \int_{\mathbb{FS}} f \, dV\,, \tag{49}$$

where $|\cdot|$ denotes the volume of the corresponding domain. After (49) is applied, the microscopic three-dimensional cell reduces to a single macroscopic point lying on a 2-manifold located at a constant distance, $d$, from a reference $(x_1, x_2)$ plane through the microstructured surface. Macroscopically speaking, since $d$ is of order $\epsilon$ and spatial variations smaller than $\epsilon$ cannot be measured by the slow variable $\mathbf{x}'$, we are allowed to take $d = 0$. As shown in [8], the present theory is not able to better estimate the value of $d$, since we are approximating the physical phenomenon at leading order in $\epsilon$. Directly linked to this fact is also the choice of $h$, the normal-to-the-surface height of the unit cell over which the variables must be averaged. Since $h$ must be of order $\epsilon$ in the present theory, we do not introduce any error by taking $h = 2\epsilon$ to include a balanced fraction of solid and fluid in the cell. Other definitions of averages can be used in order to deduce the effective quantities, starting from the microscopic tensors.

The macroscopic equations for the fluid quantities are found by applying the spatial average over the fluid domain $\mathbb{F}$ to (45) and (46), leading to

$$\langle u_i^{(0)} \rangle - \theta \frac{\partial v_i^{(0)}}{\partial t} = \int_0^t \mathcal{L}_{ijk}\, \varepsilon'_{jk}(\mathbf{u}^{out}; t') + \mathcal{H}_{ij}\, \ddot{v}_j^{(0)}(\mathbf{x}', t')\, dt'\,, \tag{50}$$

$$\langle p^{(0)} \rangle = \langle \bar{p}^{(0)}(\mathbf{x}', t) \rangle + \int_0^t \mathcal{B}_{jk}\, \varepsilon'_{jk}(\mathbf{u}^{out}; t') + \mathcal{A}_j\, \ddot{v}_j^{(0)}(\mathbf{x}', t')\, dt'\,. \tag{51}$$

with $\theta = \dfrac{|\mathbb{F}|}{|\mathbb{F} \cup \mathbb{S}|}$. The quantities $\mathcal{L}_{ijk}$, $\mathcal{H}_{ij}$, $\mathcal{B}_{jk}$ and $\mathcal{A}_j$ are defined as

$$\mathcal{L}_{ijk} = \langle L_{ijk} \rangle, \quad \mathcal{H}_{ij} = \langle H_{ij} \rangle, \quad \mathcal{B}_{jk} = \langle B_{jk} \rangle \quad \text{and} \quad \mathcal{A}_j = \langle A_j \rangle\,, \tag{52}$$

with $\mathcal{L}_{ijk}$ the *dynamic slip tensor*. To ensure uniqueness of the solution of the problems (47) and(48), we also take $\langle B_{jk} \rangle = 0$ and $\langle A_j \rangle = 0$, so that equation (51) simplifies to $\langle p^{(0)} \rangle = \langle \bar{p}^{(0)}(\mathbf{x}', t) \rangle$.

We now consider the linearly elastic solid. Equation (32) reduces to

$$\frac{\partial}{\partial x_j} C_{ijkl} \varepsilon_{kl}(\mathbf{v}^{(1)}) = 0\,, \tag{53}$$

and the interface condition (38) valid on $\partial|_{\mathbb{FS}}$ becomes

$$C_{ijkl} \varepsilon_{kl}(\mathbf{v}^{(1)}) n_j = -C_{ijkl} \varepsilon'_{kl}(\mathbf{v}^{(0)}) n_j\,. \tag{54}$$

The solution to (53) and (54) can formally be written as

$$v_i^{(1)}(\mathbf{x},\mathbf{x}',t) = \chi_i^{pq}(\mathbf{x})\,\varepsilon'_{pq}(\mathbf{v}^{(0)})(\mathbf{x}',t)\,. \tag{55}$$

Replacing (55) into (53) and (54), $\boldsymbol{\chi}^{pq}$ is found to satisfy the microscopic problem:

$$\begin{cases} \dfrac{\partial}{\partial x_j}\left\{C_{ijkl}\left[\varepsilon_{kl}(\boldsymbol{\chi}^{pq})\right]\right\} = 0 \quad \text{in} \quad \mathbb{S}\,, \\ \left\{C_{ijkl}\left[\varepsilon_{kl}(\boldsymbol{\chi}^{pq}) + \delta_{kp}\delta_{lq}\right]\right\} n_j = 0 \quad \text{on} \quad \partial|_{\mathbb{FS}}\,, \\ \chi_i^{pq} \quad \text{periodic along tangential directions 1 and 2}\,, \\ \chi_i^{pq} = 0 \quad \text{on} \quad \mathbb{B}\,. \end{cases} \tag{56}$$

Summing the dimensionless momentum equations of fluid and solid at different orders, and retaining terms up to order $\epsilon^0$ we have:

$$\epsilon^{-1}\left[\frac{\rho_s}{\rho_f}\frac{\partial\sigma_{ij}^{(1)}}{\partial x_j}\right] + \epsilon^0\left[-\frac{\partial u_i^{(0)}}{\partial t} + \frac{\partial\Sigma_{ij}^{(0)}}{\partial x_j} - \frac{\rho_s}{\rho_f}\frac{\partial^2 v_i^{(0)}}{\partial t^2} + \frac{\rho_s}{\rho_f}\left(\frac{\partial\sigma_{ij}^{(2)}}{\partial x_j} + \frac{\partial\sigma_{ij}^{(1)}}{\partial x'_j}\right)\right] = 0\,; \tag{57}$$

we then average over the total volume and, making use of Gauss' theorem and of the boundary conditions, obtain the macroscopic momentum equation for the fluid-solid composite in the form:

$$\left\{\left[\frac{\rho_s}{\rho_f} + \theta\left(1 - \frac{\rho_s}{\rho_f}\right)\right]\delta_{ij} + \mathcal{H}_{ij}\right\}\ddot{v}_j^{(0)} + \mathcal{L}_{ijk}\,\varepsilon'_{jk}(\mathbf{u}^{out}) = \frac{\rho_s}{\rho_f}\frac{\partial}{\partial x'_j}\mathfrak{C}_{ijkl}\,\varepsilon'_{kl}(\mathbf{v}^{(0)}) - \frac{1}{|\mathbb{F}\cup\mathbb{S}|}\int_{\mathbb{T}}\Sigma_{ij}^{out}\,n_j\,dA\,, \tag{58}$$

with $\mathfrak{C}_{ijpq} = C_{ijkl}\langle\varepsilon_{kl}(\chi_i^{pq})\rangle + \langle C_{ijkl}\delta_{kp}\delta_{lq}\rangle$.

Finally, we need a third equation to formally close the macroscopic problem. This is linked to the mass balance in the composite medium and is found by taking the average of (27), yielding

$$\frac{\partial\langle u_i^{(0)}\rangle}{\partial x'_i} = \varepsilon'_{pq}(\dot{\mathbf{v}}^{(0)})\,\frac{1}{|\mathbb{F}\cup\mathbb{S}|}\int_{\partial|_{\mathbb{FS}}}\chi_i^{pq}(\mathbf{x})\,n_i\,dA. \tag{59}$$

Equation (50) represents a modified boundary condition for the velocity field in the outer fluid and requires the knowledge of the solid displacement field at leading order. Thus, at each time step, the solution of (50) and (59) must be pursued to yield the unknowns $\mathbf{u}^{(0)}$ and $\mathbf{v}^{(0)}$. If the pressure $\langle p^{(0)}\rangle$ is also needed, it can be obtained through the solution of (58).

## 3. Solution of the microscopic problem and effective coefficients

In order to apply the equivalent boundary condition (50), the microscopic problems (47), (48) and (56) have to be solved. Once their solution is computed, the averaged values over a unit cell (the so-called *effective* coefficients of the microstructured elastic surface) are deduced and used in (50), (58) and (59). The computational microscopic domain used to find the solution of (47), (48) and (56) is represented in figure 2 together with a typical grid. Lengths in this figure are normalized with respect to $l$. To apply the average defined in (49), we formally set the size of the unit cell to $1\times1\times2$ in units of $l$. The results discussed below correspond to a triangular riblet-like surface with an opening angle of 90° (see figure 2). The surface over which the riblets are positioned is a plane with tangent vectors $\hat{e}_1$ and $\hat{e}_2$ and normal vector $\hat{e}_3$. The elastic solid composing the rough layer is made of an isotropic material the Poisson's ratio of which, $\nu_P$, is taken equal to 0.33. Hence the first and the second Lamé coefficients, $\hat{\lambda}$ and $\hat{G}$, are $0.73E$ and $0.38E$, respectively. The resulting dimensionless stiffness tensor $C_{ijkl}$ is, in Voigt's notation [10]

$$C_{ijkl} = \begin{pmatrix} 1.49 & 0.73 & 0.73 & 0 & 0 & 0 \\ 0.73 & 1.49 & 0.73 & 0 & 0 & 0 \\ 0.73 & 0.73 & 1.49 & 0 & 0 & 0 \\ 0 & 0 & 0 & 0.38 & 0 & 0 \\ 0 & 0 & 0 & 0 & 0.38 & 0 \\ 0 & 0 & 0 & 0 & 0 & 0.38 \end{pmatrix}. \tag{60}$$

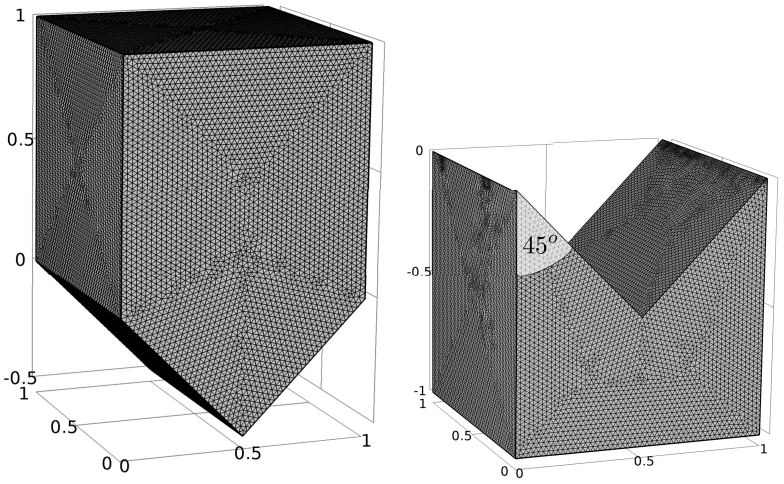


Figure 2. Typical computational grid within the $\mathbb{F}$ (left) and $\mathbb{S}$ (right) domains. With the present set up it is $\theta = 0.625$.

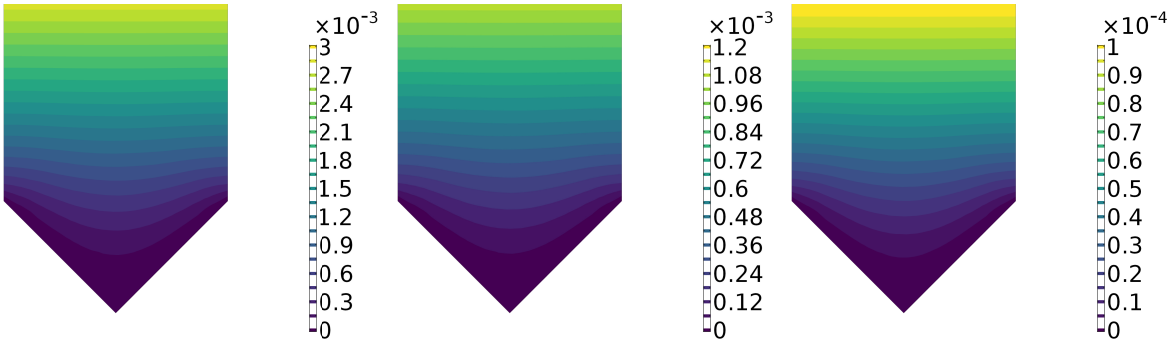


Figure 3. Time evolution of $L_{113}$. Three different time instants are shown, $t = 10, 40, 100$, from left to right, showing a decreasing behavior.

We have used the academic version of the software Comsol Multiphysics 5.3 [11] to obtain the numerical solution of the various closure problems; numerically converged results are shown below. Convergence has been checked with respect to the computational grid and also with respect to the basis functions used in the finite elements discretization implemented in Comsol (employing up to cubic polynomials for the Stokes problems in $\mathbb{F}$ and up to quintic polynomials for the solid problem in $\mathbb{S}$).

### *3.1. The convolution kernels in the fluid domain*

In this section we analyze the solution of problems (47) and (48). These are time-dependent linear Stokes problems valid over the $\mathbb{F}$ domain, with a inhomogeneous initial condition (problem 48) or inhomogeneous boundary conditions imposed on $\mathbb{T}$ (problem 47). The boundary condition on $\mathbb{T}$ for problem (47) involves a Dirac distribution which has been rendered numerically as a gaussian impulse $\mathcal{G}_\delta = \dfrac{1}{\sqrt{2\pi\delta}} e^{\frac{-t^2}{2\delta}}$. The convergence of the results by pushing $\delta$ to zero has been verified. The fact that the microstructured elastic layer is placed over a planar surface with tangent and normal vectors that do not vary in space implies that only $L_{i13}$ and $L_{i23}$ differ from zero (this was shown by Zampogna *et al.* [8] in the case of rigid microstructures). In figure 3 and 4 the relevant components of $\boldsymbol{L}$ are shown for three consecutive time-instants. The average of $\boldsymbol{L}$ plays a central role in the macroscopic model developed in the previous section, as its components represent the instantaneous slip lengths associated with the relative fluid-solid tangential velocity. In contrast, $\boldsymbol{B}$ is identically zero within the microscopic domain. After volume averaging $\boldsymbol{L}$ over the unit cell

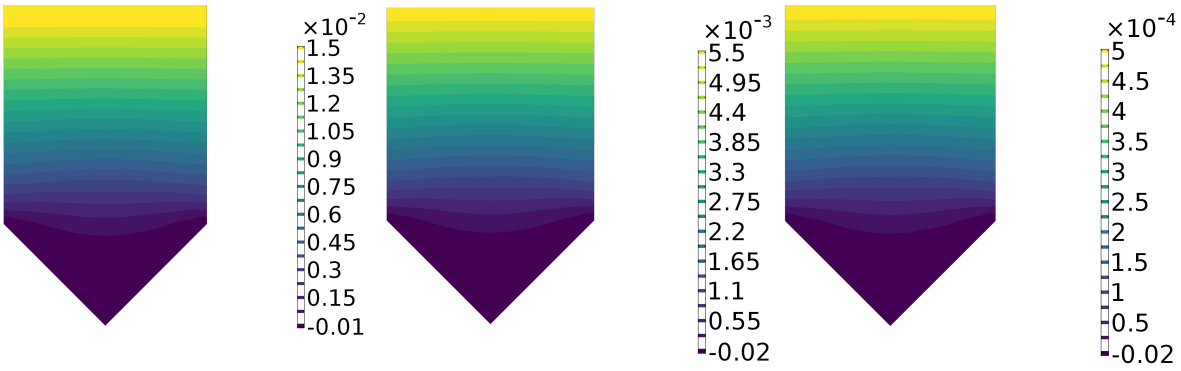


Figure 4. Time evolution of $L_{223}$. Three time instants are shown $t = 10, 40, 100$.

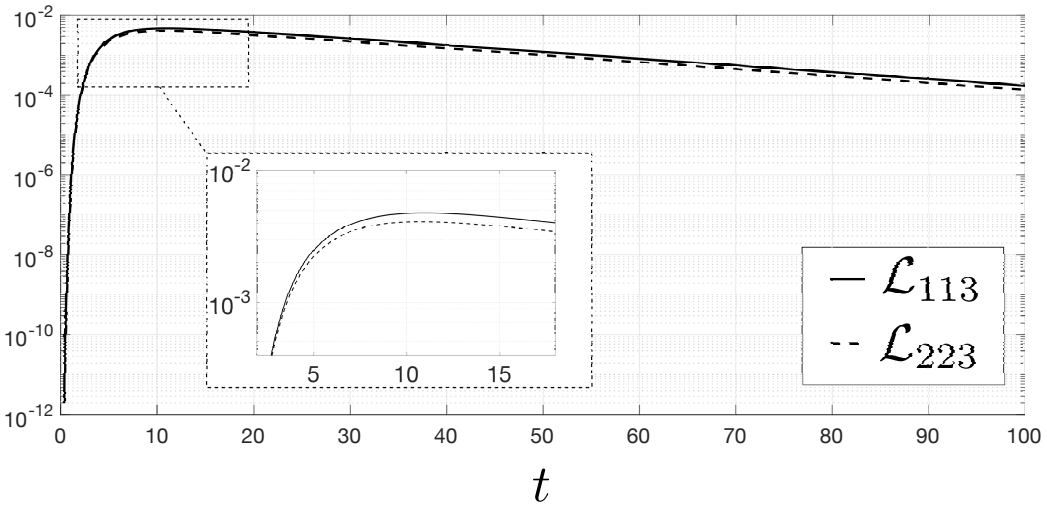


Figure 5. Time evolution of the non-zero components of $\mathcal{L}$ for a gaussian impulse centered in $t' = 0$.

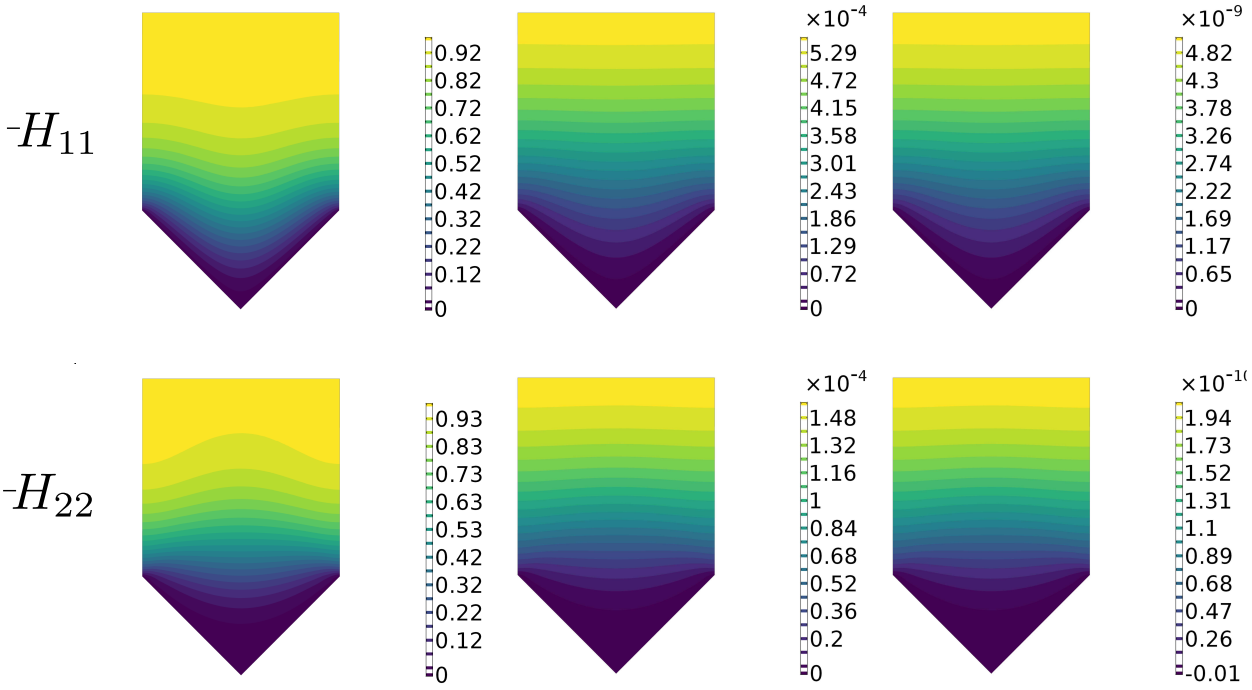


Figure 6. Non-zero components of $-\boldsymbol{H}$ for three time instants $t = 0.05, 4, 10$, from left to right.

from $x_3 = -1$ to $x_3 = 1$, the only nonzero components are $\langle L_{113} \rangle$ and $\langle L_{223} \rangle$; their behaviour in time is shown in figure 5. These components are respectively the analogous of the longitudinal and transverse slip lengths, the definition of which can be found in [2]. Similar to the conclusions of [2], they do not vary with the height of the computational cell (provided the average is always taken over the same volume, *i.e.* over a cell of dimensions $1 \times 1 \times 2$, in units of $l$). Indeed, the instantaneous averaged values obtained with the cell chosen for the present analysis remain unaltered upon increasing the height of the cell above $x_3 = 4$.

The other two tensors $\boldsymbol{H}$ and $\boldsymbol{A}$ also reach a $x_3-$ independent value for $x_3 \gtrsim 4$. While $\boldsymbol{A}$ is equal to zero within the computational domain, $\boldsymbol{H}$ (whose components are shown for three different time-instants in figure 6) has an analogous behaviour as $\boldsymbol{L}$ with two differences: it asymptotically approaches zero from the negative side and its components, in absolute values, decay to zero faster than the components of $\boldsymbol{L}$, as can be evinced from figure 7.

### *3.2. The tensor $\boldsymbol{\chi}$ in the solid domain*

The tensor $\boldsymbol{\chi}$ is the solution of a second order partial differential equation defined over the $\mathbb{S}$ domain. It represents the microscopic displacement of the structure due to internal deformations. The spatial distribution of the nonzero components of this tensor may be observed in figure 8. Most of them vanish after volume averaging, owing to their antisymmetry with respect to a vertical mid-line. All nonzero volume-averaged components are listed in table 1.

Table 1. Nonzero volume-averaged entries of the microscopic solid tensor.

| $\langle \chi_3^{11} \rangle$ | $\langle \chi_3^{22} \rangle$ | $\langle \chi_1^{13} \rangle$ | $\langle \chi_2^{23} \rangle$ | $\langle \chi_3^{33} \rangle$ |
|---|---|---|---|---|
| 0.070 | 0.072 | 0.146 | 0.146 | 0.146 |

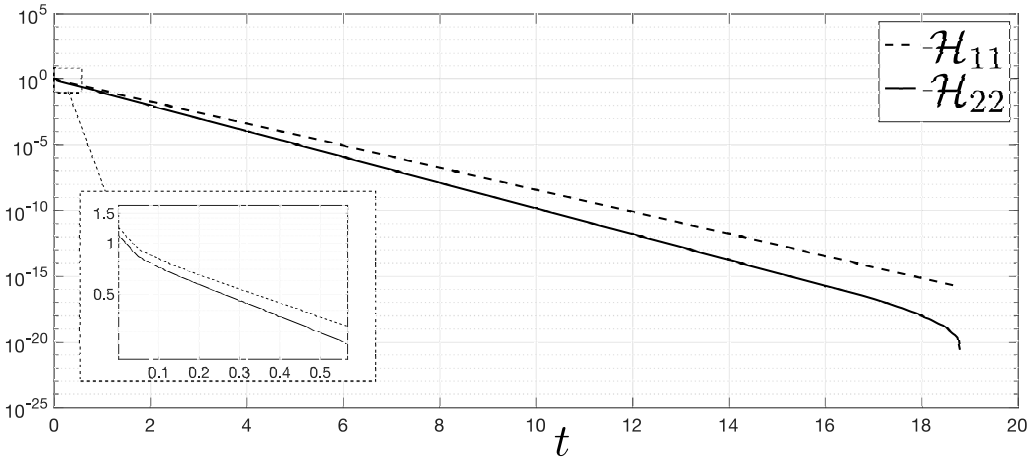


Figure 7. Time evolution of the non-zero components of $-\mathcal{H}$.

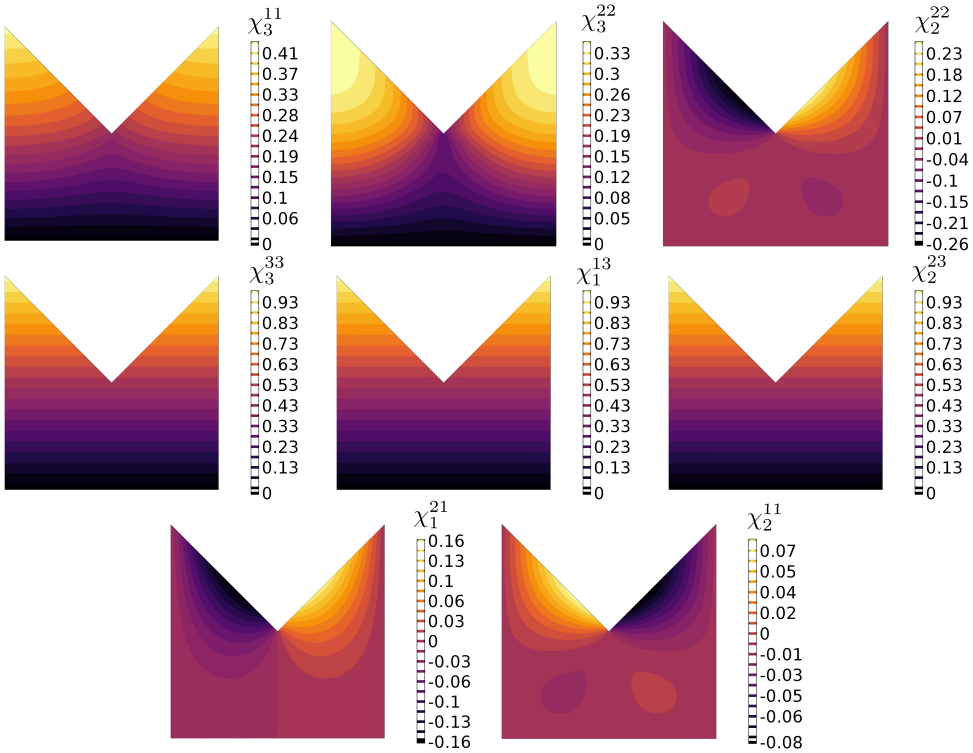


Figure 8. Non-zero components of $\chi$ on the domain $\mathbb{S}$.

## 4. Conclusions

A general framework to analyze microstructured elastic coatings anchored to a rigid, solid substrate has been presented. The lack of geometrical limitations for both the macroscopic surface and the microscopic structure makes this model suitable to explore, at a reasonable computational cost, a large number of situations involving interactions between a viscous fluid and a linearly elastic, micro-patterned surface.

Equation (50) represents a generalization of the Navier slip boundary condition for the case of deformable surfaces, rendered here by the time-convolution between the slip and the strain tensors. In this equation, the components of the tensor $\boldsymbol{L}$ are the slip lengths allowing the relative fluid-solid velocity at the equivalent surface $\mathbb{E}$ to be expressed in terms of the shear exerted by the outer flow.

## References

[1] D. W. Bechert, M. Bartenwerfer, The viscous flow on surfaces with longitudinal ribs, J. Fluid Mech. 206 (1989) 105–129.
[2] P. Luchini, D. Manzo, A. Pozzi, Resistance of a grooved surface to parallel flow and cross-flow, J. Fluid Mech. 228 (1991) 87–109.
[3] D. W. Bechert, M. Bruse, W. Hage, J. G. T. Van Der Hoeven, G. Hoppe, Experiments on drag-reducing surfaces and their optimization with an adjustable geometry, J. Fluid Mech. 338 (1997) 59–87.
[4] R. García-Mayoral, J. Jiménez, Drag reduction by riblets, Phil. Trans. Royal Soc. A 369 (2011) 1412–1427.
[5] P. Luchini, Reducing the turbulent skin friction, Computational Methods in Applied Sciences, edited by J.-A. Désideri et al., John Wiley and Sons, Chichester (1996) 466–470.
[6] P. Luchini, Structure and interpolation of the turbulent velocity profile in parallel flow, Eur. J. Mech./B Fluids 71 (2018) 15–34.
[7] D. C. Rawlings, A. G. Burg, Elastomeric riblets, United States Patent US 9,352,533 B2.
[8] G. A. Zampogna, J. Magnaudet, A. Bottaro, Generalized slip condition over rough surfaces, J. Fluid Mech. 858 (2019) 407–436.
[9] C. C. Mei, B. Vernescu, Homogenization Methods for Multiscale Mechanics, World Scientific, Singapore, 2010.
[10] W. Voigt, Ueber die beziehung zwischen den beiden elasticitatsconstanten isotroper korper, Ann. Phys. 274 (12) (1889) 573–587.
[11] COMSOL Multiphysics® v. 5.3., www.comsol.com, COMSOL AB, Stockholm, Sweden.